J Mater Sci (2009) 44:5297–5306
DOI 10.1007/s10853-009-3548-y

FERROELECTRICS

Structural defects and local chemistry across ferroelectric–electrode interfaces in epitaxial heterostructures

M. Arredondo · M. Saunders · A. Petraru · H. Kohlstedt · I. Vrejoiu · M. Alexe · D. Hesse · N. D. Browning · P. Munroe · V. Nagarajan

Received: 22 March 2009 / Accepted: 4 May 2009 / Published online: 27 May 2009

Abstract We present a detailed investigation of the chemistry at the growth interface between the bottom electrode and ferroelectric film in (001)-oriented epitaxial ferroelectric thin-film heterostructures. Three different ferroelectric systems, namely $PbZr_{0.2}Ti_{0.8}O_3$, $PbZr_{0.52}Ti_{0.48}O_3$, and $BaTiO_3$ deposited on $SrRuO_3/SrTiO_3$, were investigated to compare and contrast the role of lattice mismatch versus the volatility of the deposited cation species. A combination of transmission electron microscopy-based imaging and spectroscopy reveals distinct correlations among the ferroelectric thin-film composition, the deposition process, and chemical gradients observed across the ferroelectric–electrode interface. Sr diffusion from the electrode into the ferroelectric film was found to be dominant in $PbZr_{0.2}Ti_{0.8}O_3/SrRuO_3/SrTiO_3$ thin films. Conversely, Pb diffusion was found to be prevalent in $PbZr_{0.52}Ti_{0.48}O_3/SrRuO_3/SrTiO_3$ thin films. The $BaTiO_3/SrRuO_3/SrTiO_3$ heterostructure was found to have atomically sharp interfaces with no signature of any interdiffusion. We show that controlling the volatility of the cation species is as crucial as lattice mismatch in the fabrication of defect-free ferroelectric thin-film devices.

M. Arredondo · P. Munroe · V. Nagarajan (✉)
School of Materials Science and Engineering, University of New South Wales, Sydney, NSW 2052, Australia
e-mail: nagarajan@unsw.edu.au

M. Saunders
Centre for Microscopy, Characterisation and Analysis, The University of Western Australia, Crawley, WA 6009, Australia

A. Petraru · H. Kohlstedt
Institut für Festkörperforschung and CNI, Forschungszentrum Jülich, 52425 Jülich, Germany

I. Vrejoiu · M. Alexe · D. Hesse
Max Planck Institute of Microstructure Physics, Weinberg 2, 06120 Halle (Saale), Germany

N. D. Browning
Department of Chemical Engineering and Materials Science, University of California, Davis, CA 95616, USA

N. D. Browning
Physical and Life Sciences Directorate, Lawrence Livermore National Laboratory, Livermore, CA 94550, USA

Introduction

Thin-film ferroelectrics are now routinely used in electronic devices such as ferroelectric random access memories, RF devices, sensors, actuators, and micro-electro-mechanical systems [1]. The majority of these devices are fabricated such that the ferroelectric is deposited on a bottom electrode to provide an electrical contact for input and output data. Naturally, the performance of the device is heavily dependent on the quality of the interface between the ferroelectric and electrode/substrate heterostructure [2] where it has been shown that defects such as oxygen vacancies and cation dopants play a vital role in device reliability and endurance [3]. More recently, one singular aspect that has attracted much attention is the strong role of dislocations in the performance degradation of the ferroelectric layer [4, 5]. It has been shown theoretically that the presence of dislocations leads to polarization gradients across the ferroelectric–electrode interface and such gradients give rise to local depolarization fields that pin domain switching [5]. Typically, dislocations at the ferroelectric–electrode interface originate due to the interface (mis)-match, where the interfacial lattice misfit strain between the electrode and the

film is relaxed by the formation of edge-type misfit dislocations [6]. Another factor is the presence of growth defects such as threading dislocations that originate primarily from the substrate and composition gradients that occur as a consequence of the fabrication process and its related ambient conditions [7]. An interesting aspect of the ferroelectric–electrode interface is that by controlling the defect density, it is indeed possible to control ferroelastic (typically 90°) polydomain formation. This has been shown both theoretically [8–10] and experimentally [11] with recent results confirming that dislocations present at the ferroelectric–electrode interface can act as nucleation centers for polydomain phases [11, 12]. All of the above eventually lead to the suppression of the switchable polarization, with the case being markedly worse for ultra-thin ferroelectric thin films [5, 13] and low-dimensional ferroelectric nanostructures [4, 14]. On the other hand, it has been shown that completely defect-free model heterostructures possess excellent ferroelectric and piezoelectric properties [15].

As expected, the existing literature reflects that the quality and stability of the interface has a strong dependence on the thin-film growth process. Two widely used techniques to grow ferroelectric thin films are pulsed laser deposition (PLD) [15] and high pressure on-axis sputtering (HPOAS) [16]. Interestingly, although both techniques yield "epitaxial" samples, they differ significantly in the growth kinetics of the deposited chemical species and mean-free path of the active ions. While these techniques use deposition temperatures ($\sim$600 °C) lower than the melting temperatures of the individual constituents ($\sim$760 °C), controlling elements such as Pb can be difficult due to their high vapor pressures (i.e., high volatility). This drastically increases the probability of having compositional gradients across a given heterostructure. Therefore, optimal deposition rate and growth conditions are critical parameters to avoid these gradients.

The objective of this study is to present a systematic study of structural defects and local chemistry at the growth interface between the bottom electrode and ferroelectric film (hereafter referred to simply as the *interface*) as a function of the ferroelectric composition as well as the growth technique. Using a combination of transmission electron microscopy (TEM)-based conventional imaging and spectroscopy techniques we reveal the subtle, yet critical, differences in the chemical stability of the interface. $PbZr_xTi_{1-x}O_3/SrRuO_3$ (SRO)/$SrTiO_3$ (STO) epitaxial heterostructures with different thicknesses, deposited by PLD and HPOAS, are analyzed as our model systems. To contrast and compare the effect of Pb volatility, investigations on a Pb-free heterostructure $BaTiO_3/SrRuO_3/SrTiO_3$ deposited through HPOAS are also presented. This allows us to obtain a complete picture of the roles of parameters such as cation volatility or lattice mismatch, as a function of growth kinetics.

Experiment

To avoid complications due to grain boundaries and secondary phases we chose to focus on (001)-oriented epitaxial heterostructures. These were achieved by depositing the ferroelectric layers on perovskite oxide electrode $SrRuO_3$ (SRO)-buffered (100) $SrTiO_3$ (STO) substrates. The HPOAS SRO layers were grown at a substrate temperature and oxygen pressure of 580 °C and 3 mbar [17], respectively. For the PLD samples, the SRO layers were grown at a substrate temperature of 700 °C and an oxygen pressure of 0.14 mbar [15, 16]. Table 1 shows the growth conditions for each film, the lattice parameter at the growth temperature (T_G), and the estimated misfit with the SRO layer at T_G. The SRO layer is assumed to be pseudomorphic with the underlying STO substrate with an imposed lattice parameter at T_G of 0.393 nm [5]. The laser repetition rate used during PLD growth for both SRO and PZT 20/80 layers was 3–5 Hz [15]. The growth rate for the PZT layer varied for each technique, being 12 nm/h [17] and $\sim$200 nm/h [15] for HPOAS and PLD, respectively. Considering the critical thickness for the appearance of 90° domains [18] and dislocations (i.e., the so-called Matthews–Blakeslee critical thickness [6]), various thicknesses of the ferroelectric layers were studied to investigate the effect of each of these defects.

The local chemistry at the interface and structural defects was investigated using conventional TEM imaging

Table 1 Growth conditions, lattice parameters, and mismatches for ferroelectric layers

Ferroelectric film	Growth technique			Thickness (nm)	Lattice parameter (nm) at T_G	Misfit with SRO (%)
		T (°C)	O_2 pressure (mbar)			
PZT 20/80	HPOAS [25]	580	3	65	0.396	1 [5]
PZT 20/80	PLD [15]	575	0.3	55		
PZT 20/80	PLD [32]	600	0.4	200	0.396	1 [5]
PZT 52/48	PLD	575	0.3	200	0.4084	3.93 [5]
BTO	HPOAS [37]	700	2.6	40	0.4006	2.6 [37]

combined with energy filtered TEM (EFTEM) analysis and energy dispersive X-ray spectroscopy (EDS). Cross-sectional TEM samples were prepared by standard mechanical polishing and ion beam thinning procedures [19]. EFTEM analysis and conventional TEM imaging were performed using a JEOL 3000F operated at 300 kV, and EDS was performed using a Philips CM200 FEG TEM operated at 200 kV. Although local chemistry has been previously investigated the employing techniques such as secondary ion mass spectroscopy (SIMS) [20, 21], Auger electron spectroscopy [22], X-ray photoelectron spectroscopy [22], and X-ray diffraction [23], visual evidence of the subtle chemical changes at the interface and their dependency on interfacial defects have been difficult to obtain. This is because in the aforementioned techniques the probe size ranges from a few tens of nanometer to the order of a few microns or even larger. On the other hand, the TEM techniques used here have probe sizes of the order of a few nanometers and hence have the potential to yield more detailed and accurate spatial information on the chemical heterogeneity [21].

In addition to intrinsic instrumental limitations such as spatial resolution, signal-to-noise ratio, energy resolution, and so on [19, 24], it is critical to highlight the possible overlap of individual elemental signals in these complex-oxide heterostructures. This is a crucial factor that needs to be considered before performing any chemical mapping experiment. As an example, we consider the heterostructures used in this study. A significant overlap of the M edges occurs for Zr, Sr, and Ru in their energy loss signals used to obtain EFTEM elementals maps. This overlap is due to the signals that each element displays in the range from 200 to 500 eV extending over several hundreds of eV. The Zr-M edge commences around 200 eV and overlaps with substantial parts of both the Ru and Sr-M edges, which makes it impossible to separate the Zr signal from that of Ru and Sr. Further, for EDS analysis, the Zr-Kα peak overlaps with the edge of the Sr-Kβ peak, thus presenting a challenge to discern the start of one layer and the end of the other. This leads to an unreliable mapping for Zr using both techniques. Additionally the Ba-Lα peak overlaps with the Ti-Kα peak virtually excluding EDS analysis in this situation. Hence, to accurately map each of the constituent elements, the two techniques were exploited in a synergetic fashion. Table 2 shows the reference energies that were used for each mapping technique.

EFTEM analysis was performed using the conventional three-window method, which allows the selection of different predefined energy losses near a specific edge to generate elemental maps [24]. Both element maps and jump-ratio images were calculated. Jump-ratio images have the advantage that they display a higher signal-to-noise ratio and reduced elastic scattering contrast compared to the elemental maps. Thus, comparison of elemental maps with jump-ratio images makes it possible to discern chemical changes from elastic contrast effects [24]. Five sets of elemental maps were acquired for each sample using the three-window method and these elemental maps were compared to their respective elemental jump-ratio image. In all cases, we will present jump-ratio images so that the potential impact of elastic (diffraction) contrast is minimized, revealing the true element profiles at the interfaces.

Table 2 EELS and X-ray energies used for EFTEM and EDS [38]

Element	Z	EELS (eV)	X-ray (keV)
C	6	284 (K)	0.282 (Kα)
O	8	532 (K)	0.523 (Kα)
Ti	22	456 ($L_{2,3}$)	4.510 (Kα)
Sr	38	133 ($M_{4,5}$)	14.16 (Kα)
Zr	40	180 ($M_{4,5}$)	15.77 (Kα)
Ru	44	279 ($M_{4,5}$)	19.27 (Kα)
Ba	56	781 ($M_{4,5}$)	4.466 (Lα)
Pb	82	86 ($M_{4,5}$)	2.346 (Mα)

Heavy elements, such as Pb, can be identified through EDS [19] along with some other light elements, allowing us to corroborate the results obtained by EFTEM. The EDS data sets were acquired as continuous data points using 256 points per line, a dwell time of 2000 ms and an acquisition time of $\sim$8 min per line. Eight line scans were acquired for each element on different regions across the interface. Images were acquired before and after each line scan and no significant drift could be seen. The background was then removed to reduce noise levels and provide a more accurate qualitative reading. To improve the reliability of the EDS line scans, each scan was repeated eight times, and the presented data are a typical representative of the acquired line scans.

Results and discussion

$PbZr_{0.2}Ti_{0.8}O_3/SrRuO_3/SrTiO_3$ (PZT 20/80) system

Bright field TEM (BF TEM) was employed to investigate the interfacial quality and any structural features present. Figure 1 shows a set of BF TEM images for two PZT 20/80 samples with similar thickness of the ferroelectric layer albeit grown using different techniques. Figure 1a shows a 65-nm thick PZT film grown by HPOAS, whereas Fig. 1b shows a 55-nm thick layer grown by PLD. The 65-nm HPOAS sample displays 90° domains, threading dislocations, and a very rough SRO–PZT interface. In contrast the 55-nm PLD sample shows no domains, sharper interfaces, and a very low density of threading dislocations. This

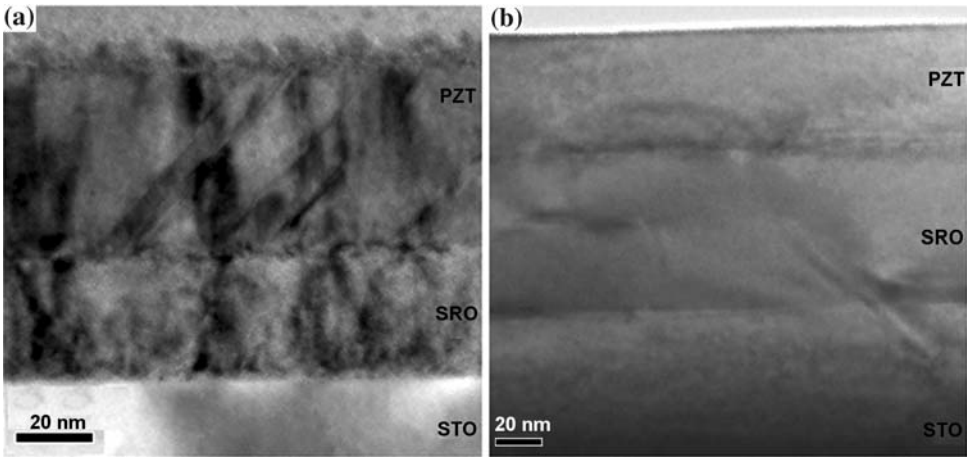

Fig. 1 Bright field images for PZT 20/80 samples: **a** 65 nm HPOAS, **b** 55 nm PLD

clearly denotes how significantly the growth conditions alone can influence the sharpness and structural defects in the heterostructures. In order to investigate the chemistry at the interface, EFTEM analysis was performed on both samples. Figure 2 shows the EFTEM data for both PZT 20/80 samples (a, c, e, and g represent data for the sputtered sample, whereas b, d, f, and h are for the PLD sample). Figure 2a, b displays the elastic images, whereas the elemental jump-ratio images are shown in Fig. 2c–h. The Sr jump-ratio maps indicate distinct Sr diffusion of ~5 nm into the PZT from the SRO for both samples (Fig. 2c, d). This is a rather unexpected result as it is conventionally thought that Ru, rather than Sr, is more susceptible to transport across the interfaces, as RuO_2 is highly volatile [25, 26]. However, earlier Cross et al. [27, 28] have published SIMS and EDS data for La-doped PZT (PLZT) on SRO that also finds Sr diffusion from SRO into the PLZT layer. They proposed that Sr diffusion is related to the excess of Pb, with such a diffusion being responsible for the high leakage current in their capacitors. It is well known that Sr doping of PZT leads to a marked decrease in the magnitude of the polarization and could also degrade the physical properties such as the dielectric constant and Curie temperature [29, 30]. This finding is critical as it provides a secondary explanation to the observed decrease in the switching polarization with decreasing thickness for Pb-based ferroelectric films [31]. Until now this has been attributed in an overwhelming majority of studies to the depolarization field at the ferroelectric–electrode interface, i.e., it is a physical effect rather than chemical roughness. The data presented in Fig. 2 demonstrate the critical need for careful examination of the chemistry of the interface and the possibility of strong "extrinsic" contributions to the observed degradation. Indeed such extrinsic factors have been thoroughly investigated for ferroelectric systems, which have a large lattice-mismatch with the underlying electrode [4, 5, 32]. The fact that Sr diffusion may occur even in what is perceived to be a perfect interface (e.g., Fig. 2b) is rather surprising.

EDS was performed to investigate Pb inter-diffusion and corroborate the results obtained by EFTEM. Figure 3 displays the EDS elemental line scans acquired across the interfaces for both samples, the dotted lines indicate the interfaces for each layer. Again the left column represents data for the sputtered sample and the right column is for the PLD sample. The EDS line scans for Sr confirm the results previously seen in the EFTEM maps of Fig. 2. They show diffusion of Sr to a distance of approximately 10 nm from the SRO into the PZT layer. Surprisingly, despite the radical (visual) difference in interface roughness between the two samples, Sr diffusion seems to be independent of interfacial sharpness or defect concentration. On the other hand, for Ti and Ru (the perovskite B-site elements) no diffusion could be measured by either technique. Neither the EFTEM results (Fig. 2e–h) nor the EDS line (Fig. 3a, b) scans for Ti or Ru indicates any movement or diffusion of the B-site species from the ferroelectric into the electrode or in the opposite direction.

To better understand the role of interfacial features in the ultimate local chemistry, we also investigated a 200-nm thick PZT 20/80 layer that was grown using PLD albeit with an oxygen-deficient target [32]. This thickness is well beyond the M-B critical thickness and was chosen so as to ensure the presence of 90° domains [18]. Figure 4a is the bright field image for this sample, which shows sharp interfaces and the expected 90° domains. Following the same methodology as above, EDS (Fig. 4b) and EFTEM (Fig. 5) analyses were performed. The EDS line scans in Fig. 4b again indicate Sr diffusion (~5 nm), while chemically sharp interfaces are observed for Ru, Ti and Pb. EFTEM maps confirm Sr diffusion into the PZT (Fig. 5b) and again, chemically sharp interfaces for B-site Ti and Ru (Fig. 5c, d). More interestingly, a closer inspection of the Sr jump-ratio image in Fig. 5b not only reveals Sr

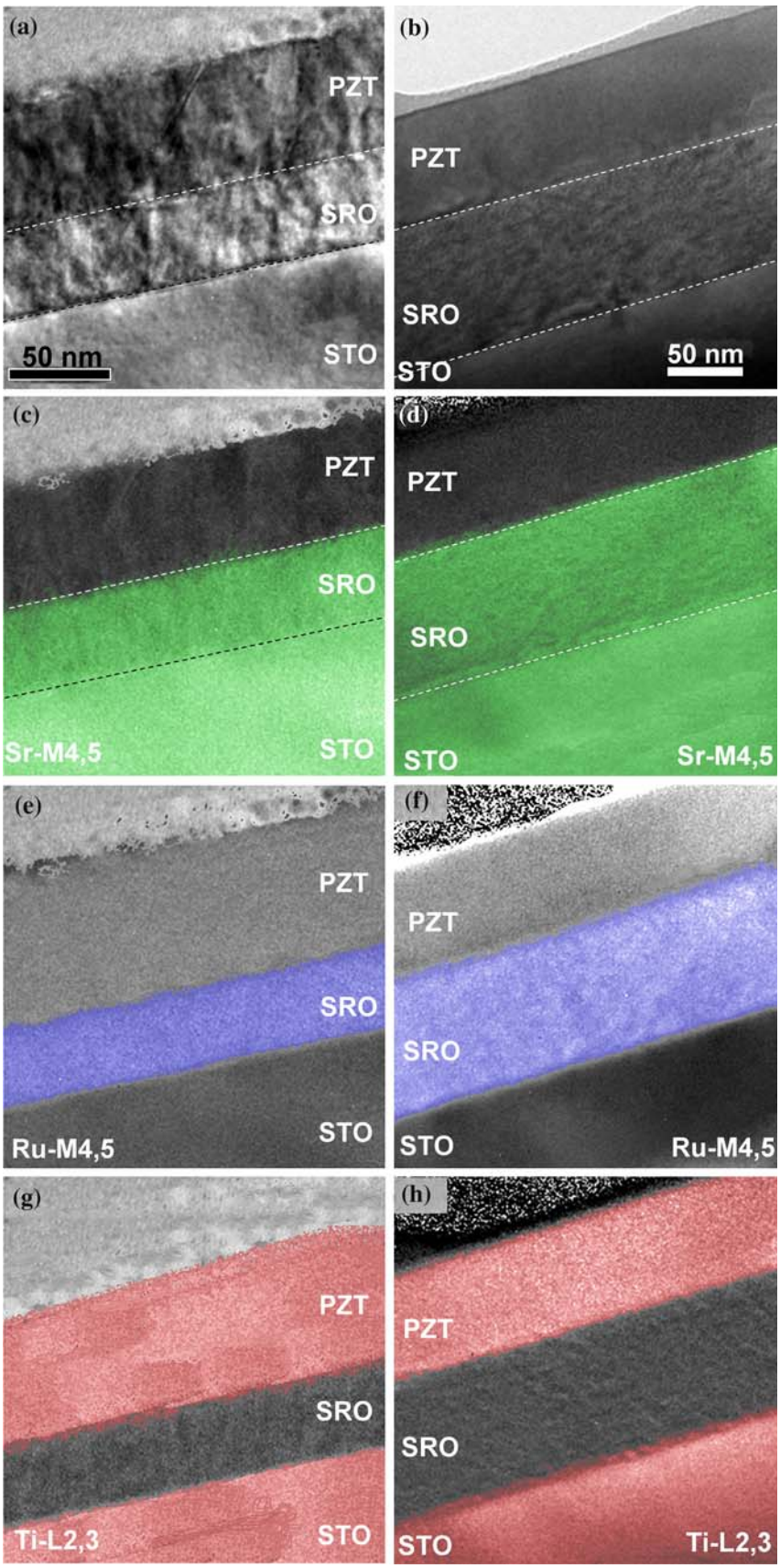

Fig. 2 EFTEM data set for PZT 20/80 samples: **a** Elastic image for 65 nm PZT 20/80 HPOAS, **b** Elastic image for 55 nm PZT 20/80 PLD, **c** Sr jump-ratio image for HPOAS sample, **d** Sr jump-ratio image for PLD sample, **e** Ru jump-ratio image for HPOAS sample, **f** Ru jump-ratio image for PLD sample, **g** Ti jump-ratio image for HPOAS sample, and **h** Ti jump-ratio image for PLD sample

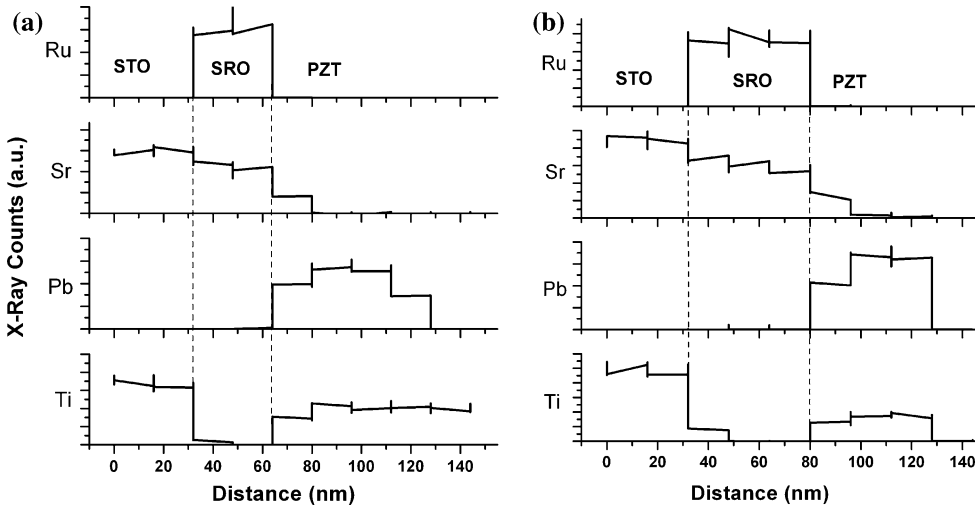

Fig. 3 EDS line scans for PZT 20/80 samples: **a** 65 nm HPOAS, **b** 55 nm PLD

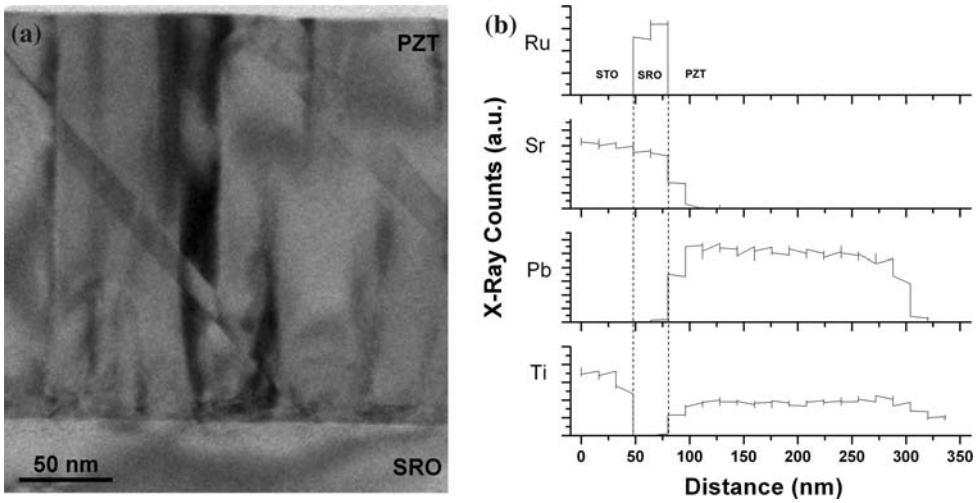

Fig. 4 PLD PZT 20/80, 200 nm: **a** Bright field image, **b** EDS line scan

diffusion, but also Sr deficiency in a region directly below the 90° domain nucleation zone, an observation hitherto unreported for PZT thin films. This deficiency is indicated by a darker contrast inside the SRO layer and highlighted by the black arrow, whereas the dotted line indicates the SRO–STO interface. Notably, although the 65-nm thick HPOAS PZT 20/80 sample showed 90° domains (Fig. 1a), it did not exhibit Sr-deficient pockets below the 90° domain nucleation zone. This latter result is unique to the thicker PZT 20/80 sample grown using the oxygen-deficient target and underlies the subtle effects of the thin-film processing conditions on the local chemistry at the ferroelectric–electrode interface. These Sr-deficient pockets are currently being examined through aberration-corrected high-resolution TEM and further investigations on the plausible mechanisms behind their origins will be reported in the near future.

It is worthwhile to note that Sr diffusion from the SRO layer into the PZT 20/80 layer is observed irrespective of the growth technique or growth rates. The next step was to quantify the extent of diffusion at the PZT/SRO interface in order to identify the driving force behind the diffusion. In epitaxial thin films, the diffusion process should be considered in terms of the main parameters that describe the mass transport phenomena, namely the diffusivity of the species and the driving force (gradient of total free energy) [29]. To identify the underpinning driving force for the cation diffusion, we examine the diffusion scenario for both Pb and Sr. As a simple approximation using parabolic kinetics typical of diffusion, the diffusion depth (X) was theoretically calculated using the formula, $X = \sqrt{Dt}$, with the diffusivity (D) calculated by the Arrhenius relationship, $D = D_o \exp(-Q/RT)$, where D_o is the diffusivity coefficient, Q the activation enthalpy, R the gas constant, and T the temperature, and t is time. We first consider the self-diffusion of Pb at 600 °C in a PLD sample, similar to that shown in Fig. 4a. Considering a total deposition time of 1 h, for Pb and using the Pb self-diffusion coefficient reported by Freer [33] for $PbTiO_3$, we find a total length $X = 60$ nm. This is more than a quarter of the thickness of

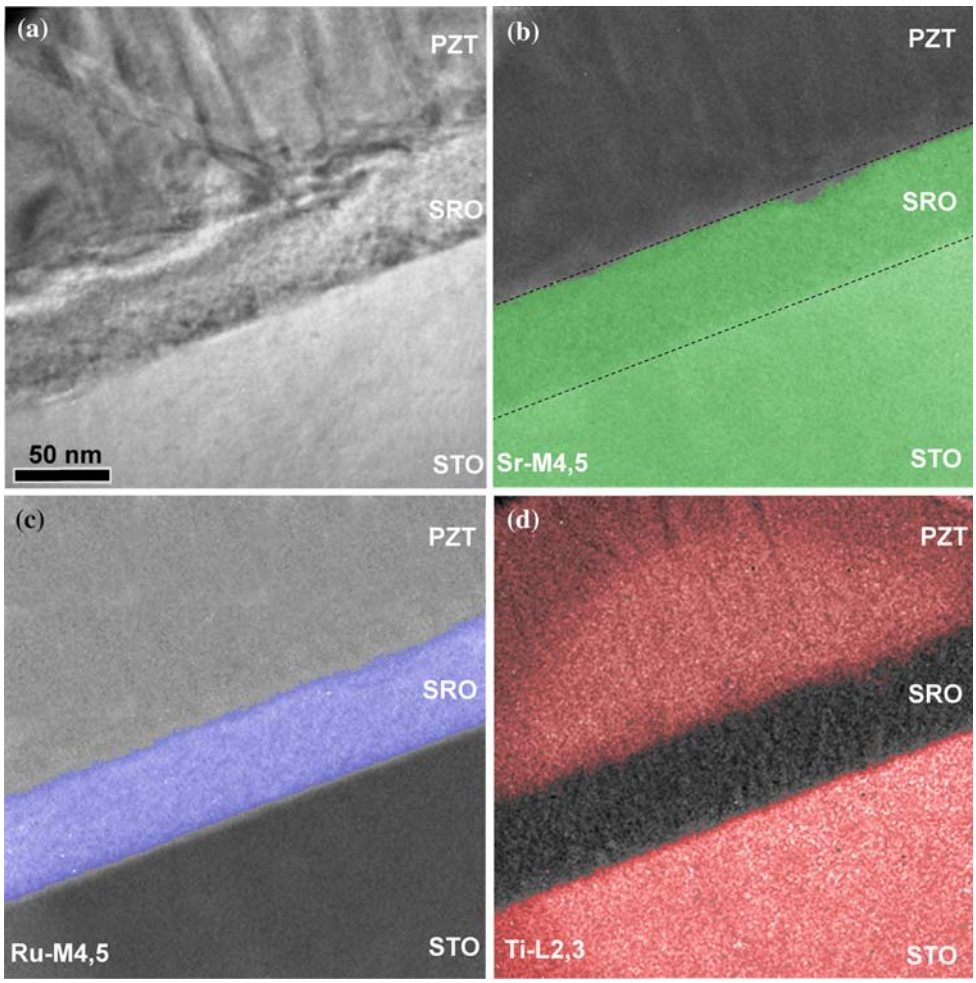

Fig. 5 EFTEM data set for PLD PZT 20/80, 200 nm (grown under non-optimal conditions [32]): **a** Elastic image, **b** Sr jump-ratio image, **c** Ti jump-ratio image, and **d** Ru jump-ratio image

the film and immediately underlines the need for excess Pb in the precursor during the growth process. More importantly under the typical vacuum and temperature conditions used for the thin-film growth process, Pb volatility is expected to worsen. The lack of dependency of Sr transport on the structural roughness of the interface and relatively tight control of the B-site ions across the interface strongly suggests that the observed Sr diffusion is driven by Pb volatility. Considering the lattice structure of PZT versus SRO, it is likely that Sr (already occupying a 2+ oxidation state A-site) would be the most ideal element to occupy the vacant Pb sites. This would hence create a diffusion process from the electrode into the ferroelectric and thus reveals the importance of chemical stability of individual elements of a heterostructure. We are able to examine this by estimating the vacancy-diffusion kinetics for Sr. The diffusivity coefficient of Sr has been reported previously for perovskite structures by several groups [34–36]. We take the value reported by Sakaguchi et al. [35] ($D_{Sr} = 3.0128 \times 10^{-21}$ m^2 s^{-1}) given for Sr diffusion into the Lead Magnesium Niobate system. Using the above diffusion coefficient and applying the parabolic law for an SRO layer grown by PLD at 700 °C gives a diffusion depth of $X = 9.5$ nm. This is in close agreement with the microscopy observations reported in the EFTEM and EDS results shown here. Although these results are quantitative approximations, they not only confirm the influence of the growth process but also the important role played by the individual chemical species.

$PbZr_{0.52}Ti_{0.48}O_3/SrRuO_3/SrTiO_3$ (PZT 52/48) system

To compare the effect of lattice mismatch, the interface for PZT 52/48 films was investigated next. The mismatch between PZT 52/48 and SRO is ~3.93% (i.e., thrice larger than in the PZT 20/80 case) and thus a high density of misfit dislocations and other mismatch accommodating defects are expected.

Although both HPOAS and PLD films were investigated, we present here the case for the PLD sample, as both datasets were identical. The bright field image (Fig. 6) for this 200-nm thick PLD PZT 52/48 sample shows that it has a high density of dislocations, very fine 90° domains and significant interface roughness, similar to the HPOAS PZT

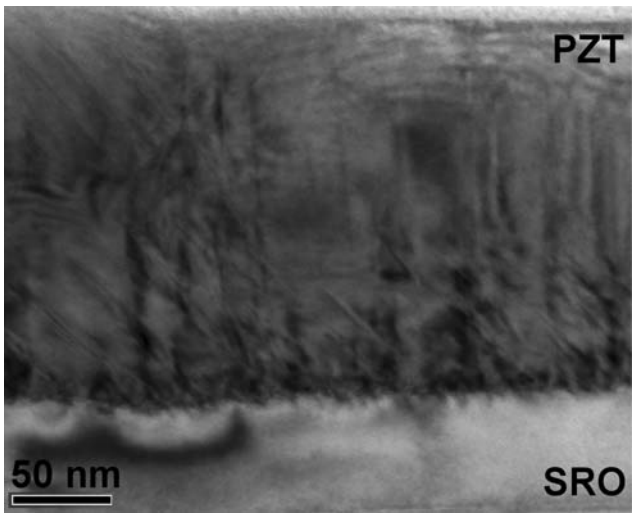

Fig. 6 Bright field image for PLD PZT 52/48, 200 nm thick

(20/80) sample. EDS analysis (Fig. 7a) now not only shows chemically sharp interfaces for Ti and Ru (as in the previous system), but also for Sr. The same Sr sharpness is confirmed by EFTEM Sr maps (Fig. 7b). On the other hand, the EDS line scans for Pb clearly show Pb diffusion into the SRO layer. Thus we have a scenario that is found to be completely opposite to that obtained in the PZT 20/80 system where evidently Sr was the element migrating into the PZT and not Pb.

To explain this strong difference, we need to consider the relevant stages of formation of misfit dislocations versus 90° domains within the ferroelectric thin film, both during the deposition process and the subsequent cooling stage. It is critical to note that growth defects such as misfit dislocations primarily nucleate at the high growth temperatures ($T_G \sim 575$–650 °C) while 90° domains are formed during the process of cooling down. It can be

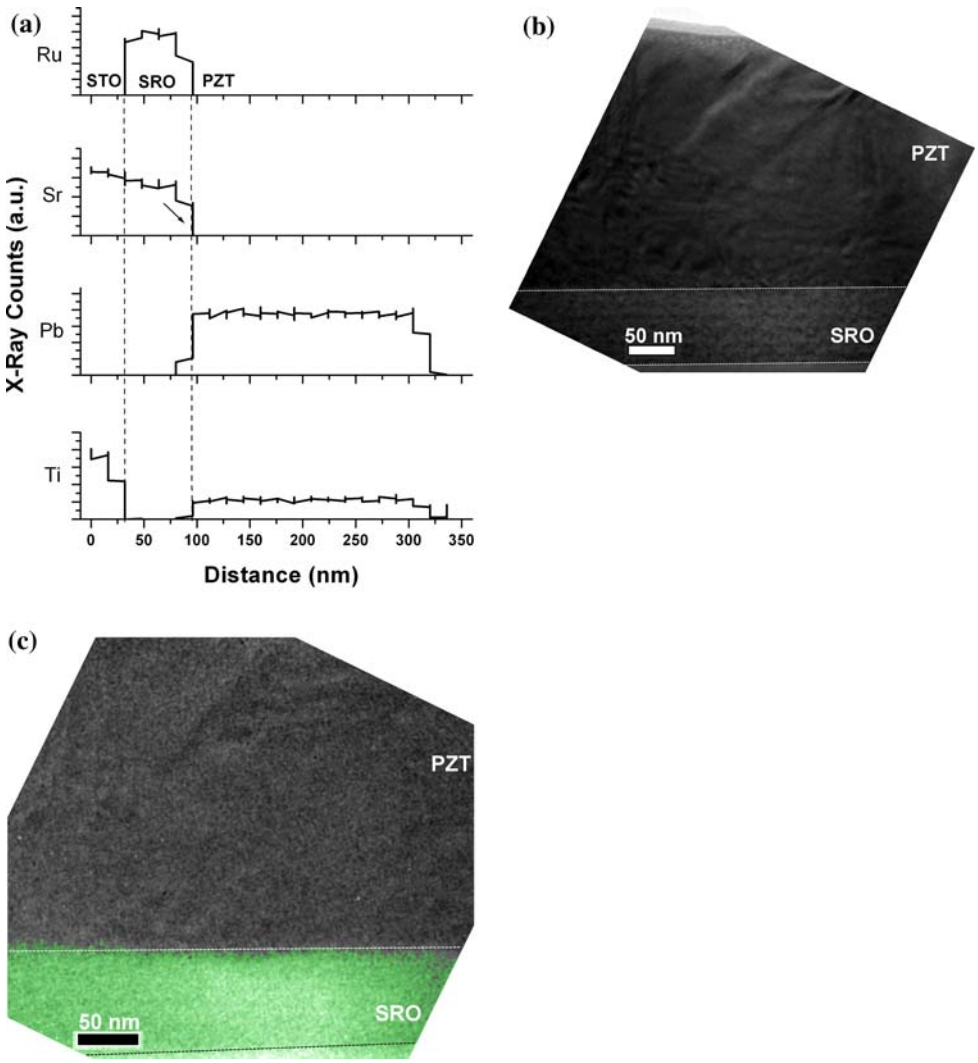

Fig. 7 PLD PZT 52/48, 200 nm: **a** EDS line scans, **b** elastic image, and **c** Sr jump-ratio map

expected that the dislocations are mobile at such high temperatures and moreover the temperatures at which dislocation formation occurs during the growth process would be typically above the Curie temperature (~400 °C for the PZT 52/48 case) and when the film is in a paraelectric state (i.e., no driving force to create ferroelastic domains). Thus for the case of the PZT 52/48 film where the interface has an extremely large density of misfit dislocations (~10^{12}/cm^2) [5], the dislocation cores can act as perfect channels for the Pb to migrate into the neighboring SRO layer. For the case of the PZT 20/80 system, the primary stress accommodating mechanism is the formation of 90° domains as the lattice mismatch is quite low (~1%). This domain formation process can occur only as the film cools down to undergo a paraelectric to ferroelectric phase transition. Thus it is possible that the nucleation of domains restricts the migration of the Pb into the SRO layer. It is also likely that the Sr penetration into the PZT 20/80 layers is a secondary stress accommodating mechanism as Sr doping into the ferroelectric layer significantly reduces the tetragonality and hence the paraelectric to ferroelectric transformation strain.

Preliminary high angle annular dark field (HAADF)/EDX results (data not shown) on a similar sample confirm several cases of diffusion of lead and titanium into SRO at the site of an interfacial dislocation. Furthermore nanoscale chemical maps of dislocation cores performed with the HAADF sample confirm that the dislocation cores do have excess Pb, with the regions in the PZT matrix directly above the core being Pb-deficient. These results are unlikely due to beam damage as we have acquired the EDS maps at an energy level of 80 to 120 kV and confirmed that the sample is undamaged by acquiring HAADF images before and after EDS analysis. More detailed HAADF imaging of dislocation cores in the 52/48 PZT sample versus the 20/80 case is currently underway and will be reported at a later stage.

$BaTiO_3/SrRuO_3/SrTiO_3$ system (BTO/SRO/STO)

Finally, we present analysis of a perfect BTO/SRO/STO heterostructure to elucidate the effect of non-volatile cations. The BTO sample was deposited by HPOAS and has a misfit of 2.6% [37]. The thickness for the BTO layer is ~50 nm and as shown in Fig. 8a has extremely smooth interfaces and no defects except for a few threading dislocations originating from the substrate. The EFTEM elemental jump-ratio images in Fig. 8c–f indicate chemically sharp interfaces for Ba, Ti, Ru, and Sr (i.e., all cation species) and hence these results are very different from the PZT systems presented before. It is worth mentioning that it is only EFTEM that identifies all the elements in the BTO heterolayer, since there is an overlap in the EDS signals for Ba and Ti, as indicated in Table 2. Nevertheless, EDS line scans were also acquired for Sr and Ru (data not shown) and they do agree with the EFTEM data. Notably, although BTO has a misfit almost twice larger than the PZT 20/80 misfit, a defect-free sample was achievable with no evidence of A-site diffusion, thus underlying the critical role of the stability/

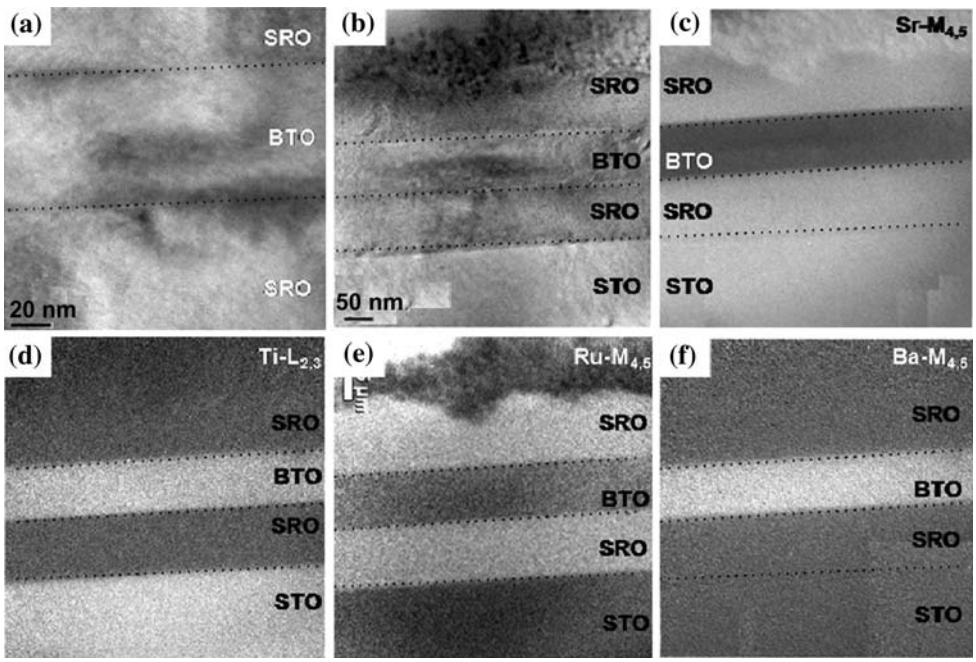

Fig. 8 HPOAS BTO, 40 nm: **a** Bright field image, **b** elastic image, **c** Sr jump-ratio image, **d** Ti jump-ratio image, **e** Ru jump-ratio image, and **f** Ba jump-ratio image

volatility of the cation species in obtaining chemically sharp interfaces.

Conclusion

We have presented detailed TEM-based investigations on three different ferroelectric systems, namely $PbZr_{0.2}Ti_{0.8}O_3$, $PbZr_{0.52}Ti_{0.48}O_3$, and $BaTiO_3$ deposited on $SrRuO_3/SrTiO_3$ in order to compare and contrast the roles of lattice mismatch versus the volatility of the deposited cation species in the chemical stability of the ferroelectric–electrode interface. A combination of imaging and spectroscopy reveals distinct interdependencies among the thin-film composition, thin-film deposition conditions as well as the nature of chemical gradients observed across the ferroelectric–electrode interface. Sr diffusion from the electrode into the ferroelectric film was found to be dominant in $PbZr_{0.2}Ti_{0.8}O_3/SrRuO_3/SrTiO_3$ thin films. Conversely, Pb diffusion was found to be prevalent in $PbZr_{0.52}Ti_{0.48}O_3/SrRuO_3/SrTiO_3$ thin films. The $BaTiO_3/SrRuO_3/SrTiO_3$ heterostructure was found to have atomically sharp interfaces with no signature of any diffusion.

Acknowledgements The authors would like to thank CONACYT (Mexico), ARC DP 0666231, the US Department of Energy through grant number DE-FG02-03ER46057, the German Science Foundation (DFG) via SFB 762 and DEST International Linkage Grant for their support on this project. We also acknowledge the facilities, scientific and technical assistance of the Australian Microscopy & Microanalysis Research Facility at the Centre for Microscopy, Characterization & Analysis, The University of Western Australia, a facility funded by The University, State and Commonwealth Governments.

References

1. Waser R (2005) Nanoelectronics and information technology: advanced electronic materials and novel devices. Wiley-VCH, Germany
2. Kang SW, Kim WK, Rhee SW (2007) J Mater Sci 42:652. doi:10.1007/s10853-006-1136-y
3. Warren WL, Tuttle BA, Dimos D (1995) Appl Phys Lett 67:1426
4. Chu MW, Szafraniak I, Scholz R et al (2004) Nat Mater 3:87
5. Nagarajan V, Jia CL, Kohlstedt H et al (2005) Appl Phys Lett 86:192910
6. Matthews JW, Blakeslee AE (1974) J Cryst Growth 27:118
7. Fitting Kourkoutis L, Muller DA, Hotta Y, Hwang HY (2007) Appl Phys Lett 91:163101
8. Emelyanov AY, Pertsev NA (2003) Phys Rev B 68:214103
9. Roytburd A (1998) J Appl Phys 83:239
10. Pompe W, Gong X, Suo Z, Speck JS (1993) J Appl Phys 74:6012
11. Venkatesan S, Vlooswijk A, Kooi BJ et al (2008) Phys Rev B 78:8
12. Misirlioglu IB, Vasiliev AL, Alpay SP, Aindow M, Ramesh R (2006) J Mater Sci 41:697. doi:10.1007/s10853-006-6488-9
13. Kornev IA, Fu H, Bellaiche L (2006) J Mater Sci 41:137. doi:10.1007/s10853-005-5962-0
14. Alexe M, Hesse D (2006) J Mater Sci 41:1. doi:10.1007/s10853-005-5912-x
15. Vrejoiu I, Le Rhun G, Pintilie L, Hesse D, Alexe M, Goesele U (2006) Adv Mater 18:1657
16. Rodrıguez Contreras J, Kohlstedt H, Petraru A et al (2005) J Cryst Growth 277:210
17. Rodriguez Contreras J, Kohlstedt H, Poppe U, Waser R, Buchal C (2003) Appl Phys Lett 83:126
18. Alpay SP, Roytburd AL (1998) J Appl Phys 83:4714
19. Williams DB, Carter CB (1996) Transmission electron microscopy. Plenum Press, New York
20. Stolichnov I, Tagantsev A, Setter N, Cross JS, Tsukada M (1999) Appl Phys Lett 75:1790
21. Kim S, Koo J, Shin S, Park Y (2005) Appl Phys Lett 87:212910
22. Zomorrodian AR, Messarwi A, Wu NJ (1999) Ceram Int 25:137
23. Hwang KS, Kim BH (1999) Mater Chem Phys 57:224
24. Verbeeck J, Van Dyck D, Van Tendeloo G (2004) Spectrochim Acta Part B Atom Spectrosc 59:1529
25. Jia CL, Contreras JR, Poppe U, Kohlstedt H, Waser R, Urban K (2002) J Appl Phys 92:101
26. Cao G, McCall S, Bolivar J et al (1996) Phys Rev B 54:15144
27. Cross JS, Fujiki M, Tsukada M, Matsuura K, Otani S (1999) Jpn J Appl Phys 2(38):L448
28. Cross JS, Fujiki M, Tsukada M et al (1999) Integr Ferroelectr 25:605
29. Gupta D, Ho PS (1980) Thin Solid Films 72:399
30. Cross JS, Fujiki M, Tsukada M, Kotaka Y, Goto Y (1998) Integr Ferroelectr 21:263
31. Ahn CH, Rabe KM, Triscone JM (2004) Science 303:488
32. Vrejoiu I, Le Rhun G, Zakharov ND, Hesse D, Pintilie L, Alexe M (2006) Philos Mag 86:4477
33. Freer R (1980) J Mater Sci 15:803. doi:10.1007/BF00552089
34. Gupta D (2005) Diffusion processes in advances technological materials. William Andrew Publishing, NY, p 489
35. Sakaguchi I, Hishita S, Haneda H (2001) Nucl Instrum Methods Phys Res B Beam Interac Mater Atoms 173:436
36. Gomann K, Bochardt G, Schulz M et al (2005) Phys Chem Chem Phys 7:2053
37. Petraru A, Kohlstedt H, Poppe U et al (2008) Appl Phys Lett 93:2902
38. Ahn CC, Krivanek OL, Burger RP, Disko MM, Swann PR (1983) EELS atlas: a reference collection of electron energy loss spectra covering all stable elements. HREM Facility, Center for Solid State Science, Arizona State University